

PNNL-34599

# Comparison of Elastic Moduli of LPBF 316H Material Using RUS Measurements and Destructive Mechanical Testing

M3CT-23PN1305091

July 2023

Robert O Montgomery  
Jared J Gillespie  
Morris S Good  
Isabella Van Rooyen

## DISCLAIMER

This report was prepared as an account of work sponsored by an agency of the United States Government. Neither the United States Government nor any agency thereof, nor Battelle Memorial Institute, nor any of their employees, makes **any warranty, express or implied, or assumes any legal liability or responsibility for the accuracy, completeness, or usefulness of any information, apparatus, product, or process disclosed, or represents that its use would not infringe privately owned rights.** Reference herein to any specific commercial product, process, or service by trade name, trademark, manufacturer, or otherwise does not necessarily constitute or imply its endorsement, recommendation, or favoring by the United States Government or any agency thereof, or Battelle Memorial Institute. The views and opinions of authors expressed herein do not necessarily state or reflect those of the United States Government or any agency thereof.

PACIFIC NORTHWEST NATIONAL LABORATORY  
*operated by*  
BATTELLE  
*for the*  
UNITED STATES DEPARTMENT OF ENERGY  
*under Contract DE-AC05-76RL01830*

Printed in the United States of America

Available to DOE and DOE contractors from  
the Office of Scientific and Technical Information,  
P.O. Box 62, Oak Ridge, TN 37831-0062

[www.osti.gov](http://www.osti.gov)

ph: (865) 576-8401

fox: (865) 576-5728

email: [reports@osti.gov](mailto:reports@osti.gov)

Available to the public from the National Technical Information Service  
5301 Shawnee Rd., Alexandria, VA 22312

ph: (800) 553-NTIS (6847)

or (703) 605-6000

email: [info@ntis.gov](mailto:info@ntis.gov)

Online ordering: <http://www.ntis.gov>

# **Comparison of Elastic Moduli of LPBF 316H Material Using RUS Measurements and Destructive Mechanical Testing**

M3CT-23PN1305091

July 2023

Robert O Montgomery  
Jared J Gillespie  
Morris S Good  
Isabella Van Rooyen

Prepared for  
the U.S. Department of Energy  
under Contract DE-AC05-76RL01830

Pacific Northwest National Laboratory  
Richland, Washington 99354



## Summary

Preliminary results are presented on the use of Resonance Ultrasound Spectroscopy (RUS) measurements of stainless steel 316H fabricated using Laser Powder Bed Fusion (LPBF) additive manufacturing methods. The elastic constants determined using RUS measurements are compared to tensile tests and RUS measurements on wrought stainless steel 316L. Good agreement is found between the RUS measurements and the mechanical testing results.

## Acknowledgments

The authors appreciate the guidance provided by Richard E. Jacob on the considerations for nondestructive evaluation (NDE) of advanced manufactured material in nuclear applications. The tensile testing was performed by Tim Roosendaal and Robert Seffens.

## Contents

Summary .....	ii
Acknowledgments .....	iii
1.0 Introduction .....	1
1.1 Background.....	1
1.2 Ultrasonic Testing in NDE of AM Materials.....	2
2.0 Ultrasonic Testing for Material Properties .....	4
2.1 Plane Wave Propagation .....	4
2.2 Resonant Ultrasound Spectroscopy and Sound Velocity.....	6
3.0 Description of the Evaluation Approach .....	8
3.1 Material and Specimen Description.....	8
3.1.1 Laser Powder Bed Fusion 316H SS .....	8
3.1.2 Wrought 316L SS .....	12
3.2 UT Sound Speed and Resonance Ultrasound Spectroscopy Setup .....	14
3.2.1 Plane Wave Velocity Measurement .....	14
3.2.2 PNNL RUS System Measurement.....	14
3.3 Mechanical Testing .....	16
4.0 Results from LPBF 316H and Wrought 316L.....	18
4.1 UT Sound Speed .....	18
4.2 Resonance Ultrasound Spectroscopy Results .....	20
4.3 Tensile Testing Results.....	25
4.4 Comparison of RUS and Tensile Testing Results.....	25
5.0 Observations and Next Steps .....	27
6.0 References .....	28
Appendix A – RUS Frequency Spectrum and Model Fit Results .....	A.1

## Figures

Figure 1. LPBF 316H Specimen from ANL.....	9
Figure 2. Scanning Electron Microscopy (SEM) images (left) and Electron Backscatter Diffraction (EBSD) images (right) both along the build direction (BD) and normal to the BD for material fabricated using the build parameters shown in Table 1. (Scale bars of 100 μm and 250 μm are shown.) .....	9
Figure 3. Sectioning plan of the LPBF 316H SS specimen. The left and right side cutting plans are not shown.....	10
Figure 4. LPBF 316H SS cuboids after being cut using electrical discharge machining.....	11
Figure 5. Wrought 316L material with cutting plan overlay. ....	12

Figure 6. EBSD image showing equiaxed grain structure with nominal grain size of about 12  $\mu\text{m}$  representative of the wrought 316 L material..... 12

Figure 7. Wrought 316L cuboids after being cut using electrical discharge machining. .... 13

Figure 8. Through transmission configuration for longitudinal (left) and shear (right) measurements. .... 14

Figure 9. A. Larger LPBF 316H and B. Smaller Wrought 316L cuboid mounted into RUS system. .... 15

Figure 10. Galaxy software with an acquired resonance from the RUS system; 135 kHz – 140 kHz frequency domain..... 15

Figure 11. Example output from RPRcode fitting the first 10 resonant frequencies and the resulting elastic moduli [Torres, 2022]. .... 16

Figure 12. Amplitude versus time plots of the ultrasonic pulses for a 2.25 MHz longitudinal wave. .... 18

Figure 13. Amplitude versus time plots of the ultrasonic pulses for a 1.0 MHz shear wave. .... 19

Figure 14. Face labeling (A) and dimensions (B) used for ultrasonic through-transmission measurements. .... 19

Figure 15. Resonant frequencies (black line) from Wrought 316L Cuboids and the identified modal peaks (red circles). .... 21

Figure 16. Resonant frequencies (black line) from LPBF 316H Cuboids and the identified modal peaks (red circles). .... 22

Figure 17. Bulk Modulus, Shear Modulus, and Poisson’s Ratio for each material and RUS model used for the four cuboids..... 24

Figure 18. Youngs Modulus for each material type and RUS model used for all cuboids compared with tensile testing of three wrought 316L specimens..... 26

## Tables

Table 1. Build Parameters for the Renishaw AM400 LPBF 316H Production ..... 8

Table 2. Measured dimensions of SS LPBF 316 H Cuboids (units in cm). .... 11

Table 3. Measured Mass and Calculated Density for LPBF 316H Cuboids ..... 11

Table 4. Measured dimensions of SS Wrought 316L Cuboids (units in cm). .... 13

Table 5. Measured Mass and Calculated Density for Wrought 316L Cuboids ..... 13

Table 6. Comparison of the ASTM E8 Subsize and the SS-J3 Tensile Specimen Geometry ..... 17

Table 7. Single-crystal elastic constants and resulting bulk elastic properties for the isotropic RUS model. .... 22

Table 8. Single-crystal elastic constants and resulting bulk elastic properties for the hexagonal RUS model. .... 23

Table 9. Mechanical Testing Results for the ASTM E8 Subsize Wrought 316L Specimens ..... 25

## 1.0 Introduction

The purpose of this report is to summarize the results from recent experiments performed to evaluate the capability of advanced ultrasonic testing (UT) techniques to interrogate and confirm the material properties and the presence of defects in components fabricated using laser powder bed fusion (LPBF). The work performed in FY23 included the application of resonant ultrasound spectroscopy (RUS) methods to measure the material elastic constants and compare the Young's modulus and Poisson's ratio to values obtained from mechanical tensile testing for both wrought 316L and LPBF 316H. One motivation of utilizing RUS is the ability to accurately estimate material elastic properties from material specimens of dimensions as small as several millimeters. Radovic et al. 2004 concluded that RUS and impulse excitation had superior precision and repeatability compared to nanoindentation and four-point bending.

The work described in this report was funded within the Advanced Materials and Manufacturing Technologies (AMMT) program within the U.S Department of Energy, Office of Nuclear Energy (DOE-NE)

### 1.1 Background

Advanced manufacturing technologies such as LPBF and Direct Energy Deposition (DED) are processes that additively layer material in a manner that can be used to fabricate components using metal powders or wire feedstock [DebRoy et al., 2018]. These processes, referred to as additive manufacturing (AM), can rapidly fabricate metal components that have complex geometries and improved material properties leading to increased design flexibility as well as cost and time savings over conventional methods. Recognizing the potential benefits of these advanced manufacturing technologies, several industries are moving forward in qualifying and deploying these methods, including fabrication of safety critical components [Todorov et al., 2014]. Key to the deployment of components produced by LPBF and DED methods is the assurance that the material conditions meet the quality and performance requirements of the application and the regulatory authorities.

The AMMT program within the U.S DOE-NE is developing materials and manufacturing technologies to support the advanced nuclear reactor design, development, and deployment [Li et al., 2022]. The major goals of the AMMT program are (1) to develop advanced materials and manufacturing technologies to support a spectrum of reactor design concepts, (2) to establish a comprehensive framework for rapid qualification of new materials made by advanced manufacturing, and (3) to accelerate commercialization of new materials and manufacturing technologies through demonstration and deployment. As part of this program, AM-based steels have been selected as a candidate manufacturing process and material to evaluate and address the scientific and technological challenges to utilization in advanced reactor applications. These challenges range from the role of powder chemistry and quality on material microstructure and component integrity, to component surface finish and dimensional accuracy, and finally, to post-process and in-service inspection considerations.

An important element in the use of components fabricated from AM processes will be the demonstration that these components are inspectable through nondestructive evaluation (NDE) methods and techniques that validate and verify quality and performance requirements [Todorov et al., 2014, Waller et al., 2014]. Post-process NDE of completed components from AM fabrication will be required to establish conformance to build requirements and to define initial conditions prior to service. In-service inspection NDE for safety critical components is an

established requirement to ensure plant safety is maintained throughout the lifetime of the component. The requirements for post-process NDE for nuclear power plant applications are described in The American Society of Mechanical Engineers Boiler and Pressure Vessel Code (ASME BPVC) Section V (Nondestructive Examination) and Section XI (Rules for Inservice Inspection of Nuclear Reactor Facility Components) and contain a wide selection of NDE techniques applicable to visual, surface, and volumetric examinations.

The main NDE methods used in the nuclear industry today are UT, radiographic testing (RT), including x-ray and gamma ray methods, visual testing (VT), penetrant testing (PT), eddy current testing (ET), and magnetic particle testing (MT) [Jacob et al. 2020]. Recent reviews of the current NDE methods and their applicability to AM materials have identified several challenges associated with complex part geometry, lack of defined defect types and size, microstructure anisotropy and nonuniformity, and lack of standard references and inspection procedures [Jacob et al., 2020, Todorov et al., 2014, and Waller et al., 2014]. These challenges are not necessarily unique to nuclear industry applications of AM components and several efforts are underway to address the NDE needs to eliminate the ambiguity in current methods to provide verification and validation approaches.

These reviews highlight several activities and technical focus areas to address the identified knowledge gaps and develop the methods and techniques to conduct reliable, effective, and safe NDE inspections of AM parts designed for advanced reactors. This project is evaluating the use of advanced UT methods for inspection of AM material properties and microstructure characterization. The recognized advantages of ultrasound measurements include the rapid and accessible approach to volumetric information from the inspection. These advantages make this method attractive for post-process and in-service NDE for AM parts.

## 1.2 Ultrasonic Testing in NDE of AM Materials

UT is a well-established and widely used NDE method that is applied in the nuclear industry for both pre-service and in-service examinations of reactor piping and components manufactured using conventional methods [Jacob et.al. 2020]. This is a volumetric method to detect and measure cracks, flaws, voids, corrosion, density, porosity, and grain structures in regions of concern, e.g., weld and heat affected zones. UT methods use a variety of techniques to apply and monitor high frequency sound waves that detect the reflections or perturbations of these sound waves from defects, flaws, or other microstructural discontinuities. Traditional UT techniques use piezoelectric transducers and a coupling medium to transmit sound waves within a material. The sound speed and the reflection of the sound waves can be used to distinguish internal features and measure elastic properties of the material. In addition to single transducers, phased-array UT systems utilize an array of transducers to guide and focus the acoustic beam throughout the component volume to increase defect detection probabilities. For non-contact UT applications, laser ultrasonics is a remote and couplant-free technique that uses lasers to generate and detect sound waves within the material and another technique is electromagnetic acoustic transducers which is a near contact technique that used electromagnetic induction.

The application of ultrasonic testing methods to material and components fabricated using AM processes has been investigated by several researchers to assess the capabilities to identify defects, evaluate porosity, and provide information on the microstructure of AM produced material [Honarvar and Varvani-Farahani, 2020, Huang et al., 2022, Kim et al., 2021 and Sotelo et al., 2021]. Both conventional and phased-array UT techniques have been used for in-process and post-process defect detection. The reflection, refraction, and scattering of acoustic waves

can provide insights into the characteristics of the material, including grain size and texture information. Another UT-based approach is RUS that utilizes acoustic energy to excite samples into the natural frequencies of elastic vibrations [Leisure and Willis, 1997]. The resonant frequencies of these elastic vibrations are defined by the sample shape, mass, and material properties. Thus, permutations that cause changes in the material properties, namely the elastic properties, can be detected using the RUS technique. The application of RUS to evaluate the material properties of AM product material and components has been explored recently as a reliable NDE method to measure the presence of porosity, cracks and grain structure variations caused by manufacturing processes changes [Garlea et al., 2019 and Manogharan et al., 2022]. The RUS method provides some advantages to more conventional UT approaches for NDE of AM components.

This report provides a summary of the recent work to apply RUS methods and mechanical testing to evaluate the elastic properties of a sample prepared from 316H material with the LPBF AM process. Section 2 provides an overview of ultrasonic behavior in materials and its relationship to intrinsic material properties. Section 3 describes the samples evaluated and an overview of the testing methods. The results are summarized in Section 4. Observations and future work are presented in Section 5.

## 2.0 Ultrasonic Testing for Material Properties

Ultrasonic techniques have proven to provide reliable and accurate measurements of the elastic properties of solids. The propagation (wave velocity) of high frequency sound waves within a material is controlled by the elastic properties of the medium. This arises due to the vibrational or oscillatory nature of the atoms as the atomic lattice responds to the applied forces. Solid materials generate several wave forms including longitudinal, shear, and surface waves. The interaction of ultrasonic vibrations with the microstructure of the material generates signatures that can provide information on the presence of local defects or distributed effects, such as grain structure or alloy content. Measurements of sound velocity and ultrasonic wave attenuation (energy loss) can be related to the elastic properties, yielding information on the key characteristics of polycrystalline metals.

The two primary ultrasonic methods to obtain information on the material properties of solid materials are to 1) measure the velocity of sound traveling through the sample (plane wave propagation) and 2) measure the resonance frequencies arising from free vibration modes. Each of these methods will be summarized below.

### 2.1 Plane Wave Propagation

Plane wave propagation is widely used to measure the ultrasonic velocity and attenuation in solids. These parameters can be related to the elastic properties of the material by using the linear elasticity stress-strain relationship given by Hooke's law. This relationship is described at the macroscopic level as:

$$\sigma = E\varepsilon \quad (1)$$

Where  $E$  is Young's modulus or modulus of elasticity for the material.

Hooke's law can also be generalized to consider the effects of material microstructure effects on the linear elasticity by applying a fourth order tensor notation for the material stiffness. This modifies Equation 1 to:

$$\sigma_{ijkl} = C_{ijkl}\varepsilon_{ijkl} \quad (2)$$

Where  $C_{ijkl}$  is the elasticity tensor.

The coefficients of the elasticity tensor describe the longitudinal and shear properties of a material in response to elastic forces. Depending on the level of symmetry of the crystallographic elements of a material, the elasticity tensor can be reduced from 81 coefficients to two (2) coefficients for isotropic materials corresponding to the elastic and shear modulus.

By utilizing solutions to the wave equation, the coefficients of the elasticity tensor can be related to the ultrasonic wave velocity within the material. From longitudinal ( $V_L$ ) and shear ( $V_s$ ) waves excited within the material, the elastic coefficients for isotropic materials are given by [Ledbetter et al., 1975, Asmani et al., 2001];

$$C_{11} = V_L^2 \rho \quad (3)$$

$$C_{44} = V_T^2 \rho \quad (4)$$

Where  $\rho$  is the material density. In isotropic materials,  $C_{44}$  is related to  $C_{11}$  and  $C_{12}$  by the following:

$$C_{44} = \frac{(C_{11} - C_{12})}{2} \quad (5)$$

The Young's modulus, shear modulus ( $G$ ), and Poisson's ratio ( $\nu$ ) can be computed from the elastic constants for isotropic material by;

$$E = \frac{3 \cdot C_{44}(C_{11} - \frac{4}{3} C_{44})}{(C_{11} - C_{44})} \quad (6)$$

$$G = C_{44} \quad (7)$$

$$\nu = \frac{(C_{11} - 2 \cdot C_{44})}{2 (C_{11} - C_{44})} \quad (8)$$

The relationships provided in Equations 3 – 8 become more complex as the amount of asymmetry within the material microstructure increases. For material produced using LPBF, a convenient representation can be to assume transversely isotropic behavior (hexagonal symmetry). A transversely isotropic material exhibits symmetry in two orthogonal planes and different behavior in the third orthogonal plane (sometimes referred to as longitudinal axis). With respect to LPBF material, the build direction may have different elastic behavior than the two planes orthogonal to the build direction. In this report, the build direction will be considered the longitudinal orientation in the transversely isotropic model. Transversely isotropic material has five (5) elastic tensor coefficients as shown [Dieulesaint and Royer, 1980]:

$$[C] = \begin{bmatrix} C_{11} & C_{12} & C_{13} & 0 & 0 & 0 \\ C_{12} & C_{11} & C_{13} & 0 & 0 & 0 \\ C_{13} & C_{13} & C_{33} & 0 & 0 & 0 \\ 0 & 0 & 0 & C_{44} & 0 & 0 \\ 0 & 0 & 0 & 0 & C_{44} & 0 \\ 0 & 0 & 0 & 0 & 0 & C_{66} \end{bmatrix} \quad (9)$$

And  $C_{66} = \frac{C_{11}-C_{12}}{2}$

The Young's Modulus (longitudinal and transverse), Shear Modulus, and Poisson's Ratio for transversely isotropic material are given by;

$$E_l = C_{33} - 2 \cdot C_{13}^2 / (C_{11} + C_{12}) \quad (10)$$

$$E_T = \frac{(C_{11} - C_{12})(C_{11} \cdot C_{33} + C_{12} \cdot C_{33} - 2 \cdot C_{13} \cdot C_{13})}{(C_{11}C_{33} - C_{13}C_{13})} \quad (11)$$

$$G_{xy} = (C_{11} - C_{12})/2 \quad (12)$$

$$\nu_L = C_{13}/(C_{11} + C_{12}) \quad (13)$$

By measuring the sound velocity in the longitudinal and transverse directions and relating to the elastic tensor coefficients, information can be obtained about the macroscopic elastic mechanical properties.

## 2.2 Resonant Ultrasound Spectroscopy and Sound Velocity

Acoustic waves propagate within solids and are affected by material properties, part geometry, and boundary conditions. Material properties include elastic moduli and density on both the microscopic and macroscopic scale. The longitudinal wave and shear wave velocities are dependent on material density and the elastic coefficients, as demonstrated by equations 3 and 4 for isotropic material. Resonance is also affected and is a phenomena of increased oscillating amplitude for a system when an applied periodic force is applied near a natural frequency of the system. One example of resonance behavior is the driven, damped harmonic oscillator which includes magnitude and the real and imaginary components of displacement. Resonance is more evident for cases where damping or loss mechanisms are small such as materials with low absorption and low scattering coefficients [Goebbels 1980]. This can be applied for either nondestructive testing (NDT) of parts or material characterization [Leisure and Willis, 1997].

RUS application to NDT is accomplished by applying a small amplitude periodic force to a part. The frequency of the applied force is swept through a defined range to acquire a resonance signature. An algorithm typically provides an objective comparison to cull out bad parts. The algorithm is constructed by a training process. An assumption is that stable and consistent resonance signatures exist for good parts and detectable changes occur for each of the flawed conditions of interest. Note that the changes can be very different depending on flaw type and the training set needs to be sufficiently large to establish representative RUS signatures of good parts and contain RUS signatures from expected flaw conditions. Due to thermal expansion and changes of material properties with temperature, compensation may be needed for temperature.

Material properties such as elastic moduli can be estimated since a material sample may be made of a precise shape and subjected to well defined environment, surface condition, and method of force application. Resonances occur for cases where constructive interference occurs which is dependent on sample dimensions, wavelength, and wave mode. Resonance frequencies of simple shapes (such as a cube, cylinder, or sphere) can be calculated by using an energy-based minimization method. Visscher et al., 1991, showed that for any free, vibrating object there exists a kinetic energy density given by

$$KE = \frac{1}{2} \rho \omega \mathbf{u}^2, \quad (14)$$

and potential energy density, given by

$$PE = \frac{1}{2} C_{ijkl} \mathbf{u}_{i,j} \mathbf{u}_{k,l} \quad (15)$$

where  $\omega$  is the frequency an object is vibrating and  $\mathbf{u}$  is the displacement of the object [Visscher, 1991]. Interestingly, Visscher showed that natural frequencies can be calculated for displacements that cause the kinetic energy density to be equal to the potential energy density

across the entire volume of the object. This relationship can be shown as an integral of the difference over a volume as

$$L = \int_V (KE - PE)dV = 0 \quad (16)$$

where L is known as the Lagrangian. Using this Lagrangian-minimization, the natural frequencies of a vibrating object with a simple shape can be calculated in terms of mass, geometry, and elastic moduli. This process of calculating the natural frequencies of an object is known as the *forward problem*.

The *inverse problem* occurs when the natural frequencies are measured for of an object with unknown elastic constants are solved for. Since the natural frequencies of an object were shown to be a function of mass, geometry, and the elastic moduli, the Lagrangian-minimization can be rearranged to create a best-fit for the experimentally measured resonances with respect to the elastic constants. This best fit is typically implemented using the Rayleigh-Ritz method. This method requires an initial guess for the elastic moduli and then the elastic moduli are iteratively solved for using a least-squares minimization method [Leisure and Willis, 1997].

### 3.0 Description of the Evaluation Approach

This section describes the evaluation approach used to assess the abilities of advanced ultrasonic methods to yield information on the material microstructure of stainless steel (SS) 316H produced using LPBF processes. The approach included sample acquisition, specimen fabrication, plane wave propagation measurements, RUS measurements, and mechanical testing.

#### 3.1 Material and Specimen Description

Two materials were selected to perform elastic modulus assessments using advanced ultrasonic methods for comparison to the mechanical measurements. These are:

- LPBF 316H SS
- Wrought 316L SS

A brief description of the material is provided in the following sections.

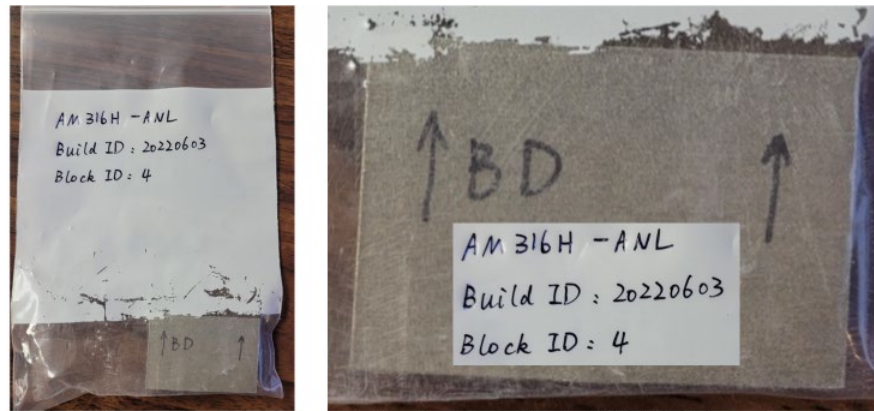
##### 3.1.1 Laser Powder Bed Fusion 316H SS

A sample of LPBF SS 316H was obtained from Argonne National Laboratory (ANL) that measured approximately 1 cm x 4 cm x 2.54 cm. The LPBF process parameters are shown in Table 1 and a picture of the sample (labeled Block ID #4) is shown in Figure 1. ANL performed microstructural characterization and the results are shown in Figure 2.

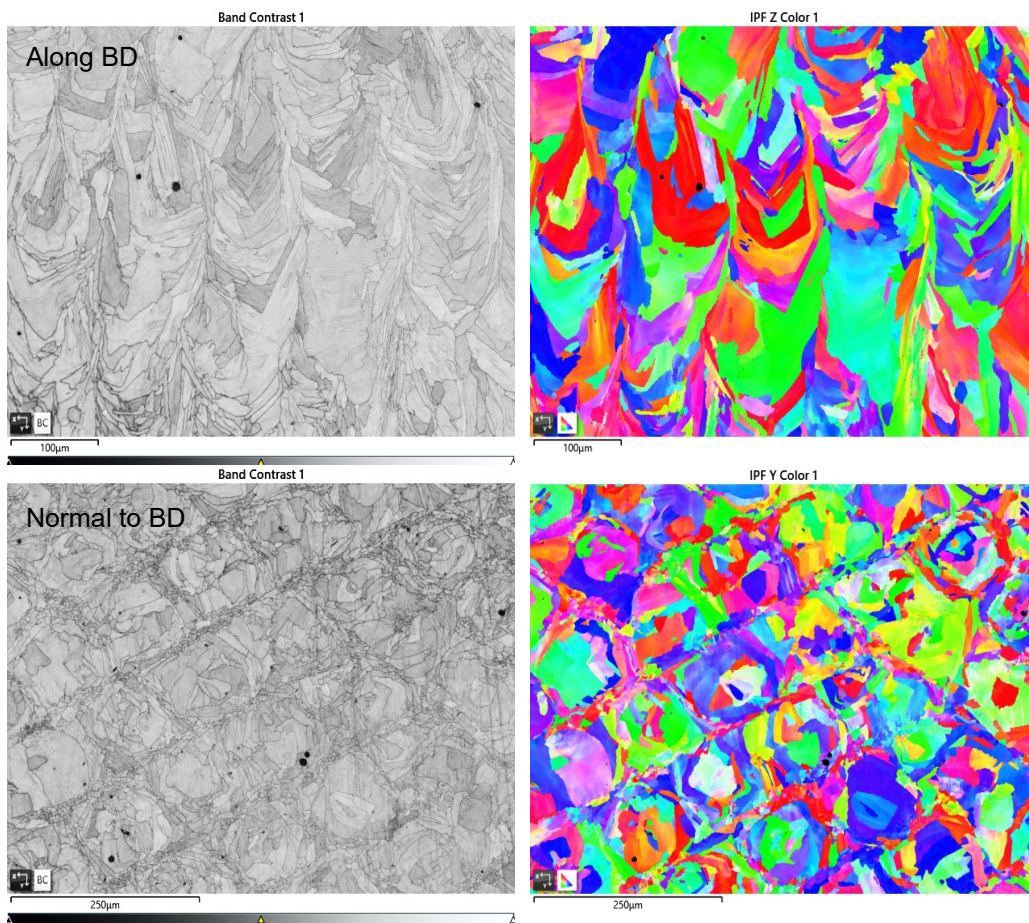
As can be seen in the metallographic examination results in Figure 2, the LPBF 316H material exhibits a nonuniform grain structure with a layered microstructure with elongated columnar features parallel to the build direction (BD). This arises from the melting process of the powder layer as the laser moves past. The microstructure orthogonal to the build direction shows a more uniform grain microstructure that matches closely the hatch spacing (~110 micrometers) of the laser. This complex microstructure is expected to impact the mechanical properties of the material.

Table 1. Build Parameters for the Renishaw AM400 LPBF 316H Production

Build ID	Material	Nominal Part Dimensions	Scan Strategy	Laser Power (W)	Point Distance (μm)	Exposure Time (μs)	Hatch Spacing (μm)	Rotation Angle (deg)	Layer Height (μm)
20220603	316H	1 cm x 4 cm x 2.54 cm	Meander	195	60	80	110	67	50



A. Part in sealed bag. B. As Received AM316 H Specimen.  
**Figure 1. LPBF 316H Specimen from ANL**



**Figure 2. Scanning Electron Microscopy (SEM) images (left) and Electron Backscatter Diffraction (EBSD) images (right) both along the build direction (BD) and normal to the BD for material fabricated using the build parameters shown in Table 1. (Scale bars of 100 µm and 250 µm are shown.)**

A sectioning plan for the as-received LPBF 316H SS specimen was developed to generate RUS cuboid samples and mechanical tensile specimens. The section plan and sample numbering scheme is shown in Figure 3. Specimens fabricated from this part included four small cuboids to

provide RUS measurements and 28 tensile test specimens. The dimensions for the RUS cuboids were defined based on an optimization analysis to be 8 mm x 9 mm x 10 mm to yield appropriate frequency modes.

The tensile specimens shown in Figure 3 were prepared using nominal dimensions based on the miniature SS-J3 geometry [Gussev et al., 2014]. The thickness of the SS-J3 tensile specimens are nominally 1 mm and the width of the gauge section is ~1.2 mm.

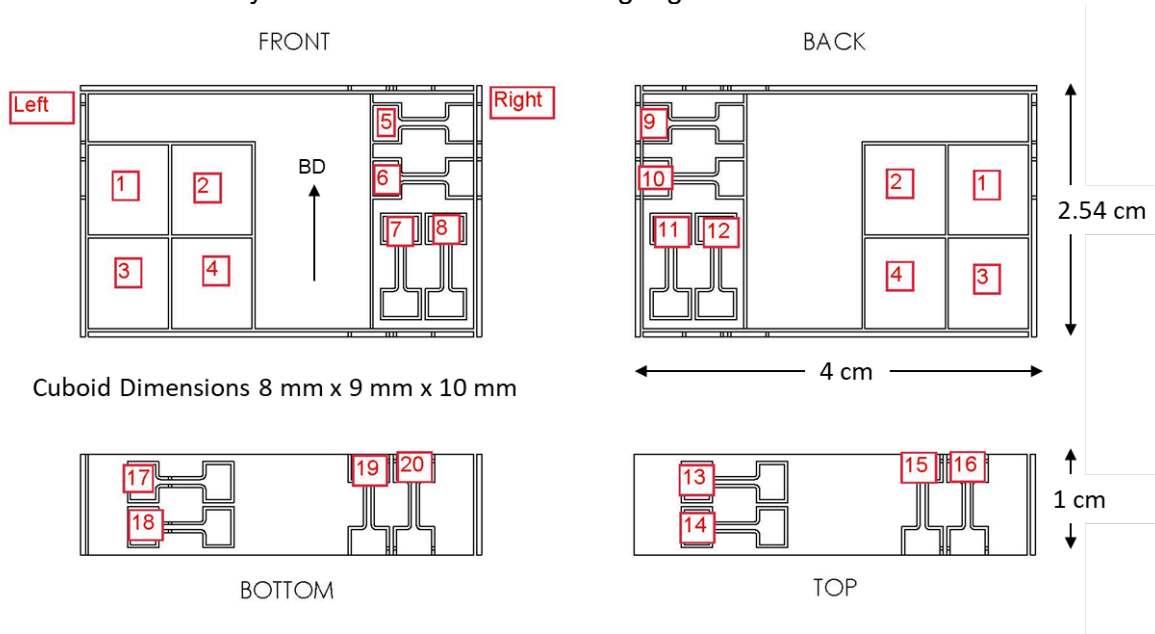


Figure 3. Sectioning plan of the LPBF 316H SS specimen. The left and right side cutting plans are not shown.

The cuboids were in the configuration shown in Figure 3. This resulted in the front and back faces being uncut while the bottom, top, and side faces were machined (see Figure 4). The mass and dimensions of each cuboid were measured using a Mettler Toledo MS204 scale and Mitutoyo CD-6" ASX digital calipers, respectively. In order to ensure that the faces of the cuboids were parallel, the four edges between the faces were measured. If the faces are not parallel than the edge lengths would not be the same value. Table 2 shows the four (4) edge measurements for each of the three (3) coordinate axes with each cuboid. The resulting standard deviation was below 10  $\mu\text{m}$ , an acceptable tolerance for RUS, for all but Cuboid 1 in the Y-direction, Cuboid 2 in the X-direction, and Cuboid 4 in the Y-direction. These four measurements were averaged for each cuboid to provide more reliable dimensional measurements in the RUS model.

The measured mass and the calculated volume and density of each cuboid is shown in Table 3. The variation the calculated density between the cuboids is less than 0.5%.



Figure 4. LPBF 316H SS cuboids after being cut using electrical discharge machining.

Table 2. Measured dimensions of SS LPBF 316 H Cuboids (units in cm).

Axis	Cuboid	Edge 1	Edge 2	Edge 3	Edge 4	STD	Mean
x	1	0.8001	0.7988	0.8001	0.7988	6.35E-04	0.7995
	2	0.8026	0.8039	0.8052	0.8052	1.05E-03	0.8042
	3	0.8001	0.8001	0.8001	0.7988	5.50E-04	0.7998
	4	0.8052	0.8052	0.8052	0.8039	5.50E-04	0.8049
y	1	0.8979	0.8992	0.9004	0.9004	1.05E-03	0.8995
	2	0.8979	0.8979	0.8979	0.8979	0.00E+00	0.8979
	3	0.9030	0.9030	0.9030	0.9042	5.50E-04	0.9033
	4	0.9030	0.9055	0.9081	0.9042	1.88E-03	0.9052
z	1	1.0033	1.0033	1.0033	1.0020	5.50E-04	1.0030
	2	1.0008	1.0008	1.0008	1.0020	5.50E-04	1.0011
	3	1.0033	1.0033	1.0020	1.0020	6.35E-04	1.0027
	4	1.0020	1.0020	1.0008	1.0008	6.35E-04	1.0014

Table 3. Measured Mass and Calculated Density for LPBF 316H Cuboids

Cuboid	Mass (g)	Volume (cm <sup>3</sup> )	Density (kg/cm <sup>3</sup> )
1	5.7591	0.7212	7.9849
2	5.7965	0.7229	8.0186
3	5.7815	0.7244	7.9815
4	5.8304	0.7296	7.9915

### 3.1.2 Wrought 316L SS

Because of the limited amount of LPBF material available for testing, an alternative material was obtained to develop the mechanical testing and RUS methods used in the project. Wrought SS 316L was identified as a candidate surrogate material and a specimen was found in another program at PNNL that had previously been characterized. The amount of material available allowed for the fabrication of American Society for Testing and Materials (ASTM) E8 sub-sized tensile specimens in addition to the cuboids and SS-J3 specimens shown in Figure 3. Figure 5 is an image of the wrought 316L material with the cutting plan overlayed. Microstructural characterization of the wrought 316L material is shown in Figure 6. Equiaxed grain structure is shown with a nominal value of about 12 micrometers.

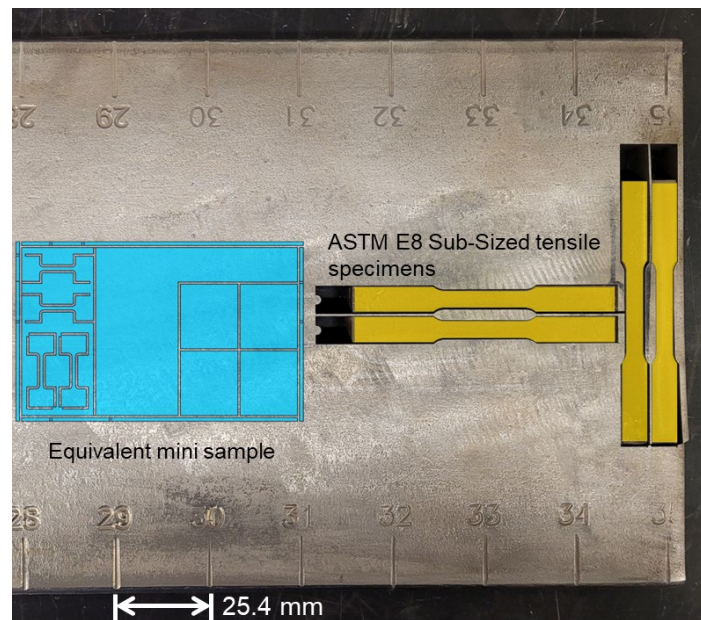


Figure 5. Wrought 316L material with cutting plan overlay.

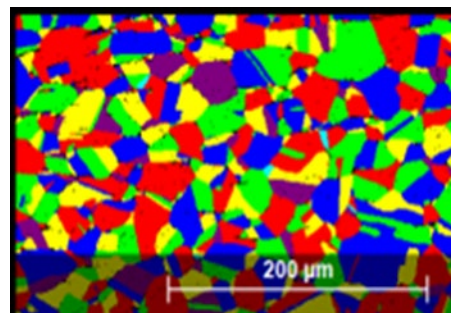


Figure 6. EBSD image showing equiaxed grain structure with nominal grain size of about 12  $\mu\text{m}$  representative of the wrought 316L material.

The wrought 316L sample was cut into 4 cuboids in the same orientation and size as the 316H LPBF sample (shown in Figure 7). The mass and dimensions were also measured in the same manner as the LPBF samples (Table 4). All but Cuboid 1 in the Y-direction was below 10  $\mu\text{m}$

standard deviation which indicates that the faces are parallel. The mass and calculated density for each cuboid are shown in Table 5. Interestingly, the density for Cuboid 3 is slightly less than that of the other cuboids. It is unclear why this is the case.



Figure 7. Wrought 316L cuboids after being cut using electrical discharge machining.

Table 4. Measured dimensions of SS Wrought 316L Cuboids (units in cm).

Axis	Cuboid	Edge 1	Edge 2	Edge 3	Edge 4	STD	Mean
x	1	0.9017	0.9004	0.9017	0.9017	5.50E-04	0.9014
	2	0.9017	0.9004	0.9004	0.9004	5.50E-04	0.9007
	3	0.7988	0.8001	0.7988	0.7976	8.98E-04	0.7988
	4	0.8014	0.8001	0.8001	0.8014	6.35E-04	0.8007
y	1	0.8001	0.7976	0.7988	0.8001	1.05E-03	0.7991
	2	0.8026	0.8014	0.8014	0.8014	5.50E-04	0.8017
	3	0.8992	0.9004	0.8992	0.8979	8.98E-04	0.8992
	4	0.8966	0.8966	0.8966	0.8954	5.50E-04	0.8963
z	1	1.0173	1.0185	1.0173	1.0173	5.50E-04	1.0176
	2	1.0173	1.0173	1.0173	1.0173	0.00E+00	1.0173
	3	1.0173	1.0173	1.0185	1.0173	5.50E-04	1.0176
	4	1.0173	1.0173	1.0185	1.0173	5.50E-04	1.0176

Table 5. Measured Mass and Calculated Density for Wrought 316L Cuboids

Cuboid	Mass (g)	Volume (cm <sup>3</sup> )	Density (g/cm <sup>3</sup> )
1	5.8277	0.7330	7.9504
2	5.8530	0.7346	7.9677
3	5.7992	0.7309	7.9342
4	5.8232	0.7303	7.9735

## 3.2 UT Sound Speed and Resonance Ultrasound Spectroscopy Setup

Ultrasonic sound velocity and RUS were used for material characterization of multiple stainless-steel samples. A brief overview of each method is provided.

### 3.2.1 Plane Wave Velocity Measurement

The plane wave velocity measurements used a through-transmission configuration to transmit an ultrasonic wave across either the length, width, or height of a specimen as shown in Figure 8. Three measurements were acquired for longitudinal waves (L-waves) and six for shear waves (S-waves) because of polarization parallel and perpendicular to sample faces. Coupling inconsistency between transducers and a sample cause response amplitude fluctuations. S-waves are particularly sensitive to this since a viscous liquid is needed to couple shear stress between the two and the increased viscosity typically increases amplitude variations.



Figure 8. Through transmission configuration for longitudinal (left) and shear (right) measurements.

### 3.2.2 PNNL RUS System Measurement

RUS data was collected with a Quasar International, Inc. Model RI-2000 transceiver and two corresponding transducers. A specimen was placed between the two RUS transducers with diametrically opposite corners of the specimen in contact with the RUS transducers (Figure 9). Frequency domains of 20 kHz – 200 kHz and 135 kHz – 350 kHz were used for the larger samples and the smaller cuboids, respectively. Frequency bands were subjectively determined so that resonance groupings permitted low amplitude and high amplitude measurements by selecting an attenuation setting for each band, so measurements remained in the linear range of the instrument and enabled good signal-to-noise (SNR) for both low and high amplitude resonances.



A. Larger sample (LPBF 316H)      B. Smaller cuboid(Wrought 316L)

Figure 9. A. Larger LPBF 316H and B. Smaller Wrought 316L cuboid mounted into RUS system.

The transceiver was controlled using Galaxy RI2000, an acquisition software designed Quasar International for taking RUS measurements (see Figure 10). The software communicates directly with the transceiver and allows a frequency domain, denoted as a band, to be specified for data acquisition. The software will then sweep through the frequency domain at a specified step resolution (units Hz). The dwell parameter specifies how long before moving from a step to another. In general, a smaller step size and higher dwell time will result in a better SNR with the tradeoff of a longer interim for data acquisition.

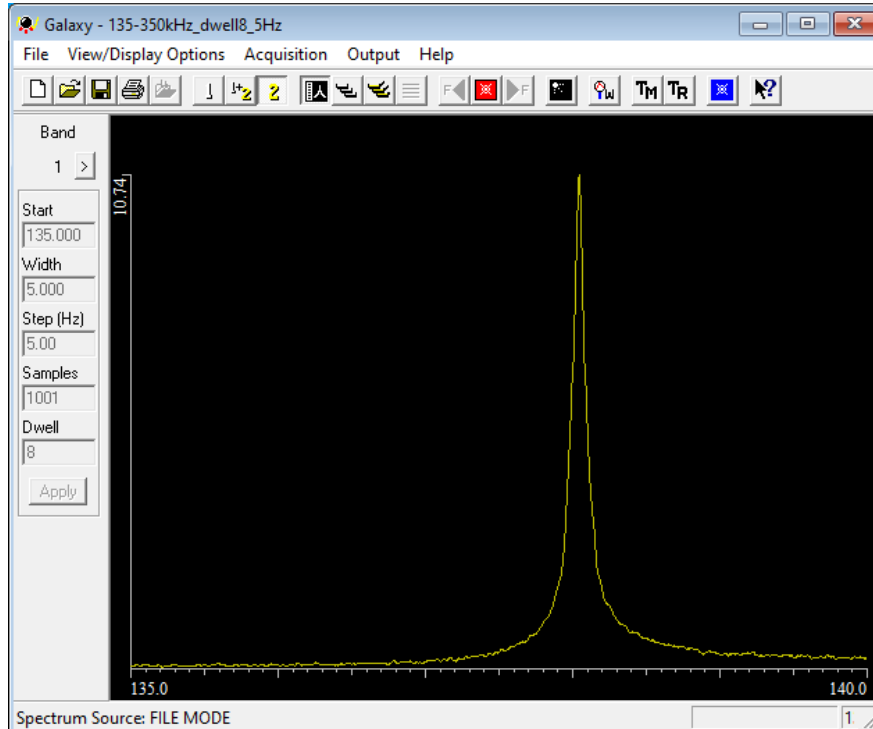


Figure 10. Galaxy software with an acquired resonance from the RUS system; 135 kHz – 140 kHz frequency domain.

Los Alamos National Laboratory (LANL) RPRcode Version 6.0 was used to calculate the expected resonance frequencies and fit the elastic constants to the experimentally measured frequencies (the forward and inverse problem) [Torres, 2022]. A typical output from the RPRcode is shown in Figure 11. First, the RPRcode is run to calculate a certain number of resonance frequencies for the given sample geometry, mass, and predicted elastic constants. Next, the measured resonances are added to the output of the first run and the code is set to fit the data by “freeing up” the elastic constants according to the selected crystal symmetry. The supported symmetries are isotropic, cubic, hexagonal, tetragonal, and orthorhombic. After a good fit is achieved, the Young’s modulus, bulk modulus, and Poisson’s ratio can be calculated using Equations (6), (7), and (8).

```

LANL RPRcode Ver. 6.0
RUS-LPBF-316H-SS-Cuboid-01_02
free moduli are c11, c44
using 12 order polynomials    mass= 5.7591 gm  rho= 7.984 gm/cc

n    fex    fr    %err wt  k  i    df/d(moduli)
1  0.138420 0.137217 -0.87 1.00 4  1  0.00  1.00
2  0.176025 0.176227  0.11 1.00 4  2  0.00  1.00
3  0.185460 0.185425 -0.02 1.00 1  2  0.08  0.92
4  0.194795 0.194545 -0.13 1.00 6  2  0.12  0.88
5  0.204020 0.202357 -0.82 1.00 8  2  0.01  0.99
6  0.213100 0.215037  0.91 1.00 3  2  0.01  0.99
7  0.223765 0.223933  0.08 1.00 7  2  0.07  0.93
8  0.225385 0.225087 -0.13 1.00 2  2  0.01  0.99
9  0.226730 0.226295 -0.19 1.00 5  1  0.02  0.98
10 0.231700 0.230982 -0.31 1.00 1  3  0.31  0.69

Bulk Modulus= 1.5810

    c11    c22    c33    c23    c13    c12    c44    c55    c66
2.59074 2.59074 2.59074 1.07619 1.07619 1.07619 0.75727 0.75727 0.75727

    d1    d2    d3
0.79950 1.00300 0.89950
|
loop# 3 rms error= 0.3900 %, changed by 0.0000001 %

length of gradient vector= 0.000000 blamb= 0.000000

eigenvalues          eigenvectors
    0.03034    1.00 0.03
    20.60846   -0.03 1.00

chisquare increased 2% by the following % changes in independent parameters
0.95 -0.10
0.00 0.12

```

Figure 11. Example output from RPRcode fitting the first 10 resonant frequencies and the resulting elastic moduli [Torres et al., 2022].

### 3.3 Mechanical Testing

An alternative method to measure the elastic properties of the samples is to perform tensile testing and use the slope of the resulting stress-strain response within the elastic regime to obtain the Young’s Modulus. A series of tensile tests with the SS-J3 specimen design were performed. ASTM E8 sub-sized tensile specimens for the 316L material were also tested to confirm the results from the SS-J3 specimen. A comparison of the ASTM E8 subsize and SS-J3 tensile specimens is shown in Table 6 [Gussev et al., 2014].

Table 6. Comparison of the ASTM E8 Subsize and the SS-J3 Tensile Specimen Geometry

Specimen Dimension	ASTM E8 Subsize Specimen (mm)	SS-J3 Specimen (mm)
Gauge Length	25.0	5
Width	6.0	1.2
Thickness	6.0	<1.0
Overall Length	100.0	16.0
Fillet radius	6.0	1.4
Grip Width	10.0	4.0

Specimens were tested on an Instron 5582 servo-mechanical testing system with Bluehill Universal control software. The test was conducted following applicable sections of ASTM E8 and specimens were fixtured to allow the gauge of the specimen be visible to the digital image correlation (DIC) system. The DIC system consisted of Correlated Solutions' VIC-Snap acquisition software, a micro-DIC camera system with BX51 stereoscope and custom beam splitter, 5 MP cameras, and a National Instruments data acquisition (DAQ). Load data from a 5kN load cell was collected with the DAQ and synchronized with the image acquisition for calculating stress values. The DIC system was setup with a 5 mm field of view to analyze the gauge section of the specimen. The speckle pattern was applied to the specimen using an airbrush with black pain on white background. Images were analyzed with a 99 pixel (px) subset size and 29 px step size. The average axial strain in the center of the specimen gauge section was used to export stress-strain data for calculating Young's Modulus according to ASTM E111.

The methodology described in ASTM E111 was used to extract the Young's Modulus from the load-displacement data. This methodology uses a least-squares regression analysis to obtain the Young's Modulus for both loading and unloading conditions. High resolution strain data from the DIC system provided approximately 180 data points for use in the regression analysis.

## 4.0 Results from LPBF 316H and Wrought 316L

Preliminary results from the ultrasonic testing and mechanical tensile tests are provided in this section.

### 4.1 UT Sound Velocity

The ultrasonic wave velocity methods summarized in Section 3 were applied to the LPBF SS 316 H sample from ANL (Block 4) prior to sectioning for RUS and tensile testing. The results for the L-wave measurements are shown in Figure 12. The S-wave measurements are shown in Figure 13. The face labeling and sample orientation is shown in Figure 14.

Multiple means exist to estimate wave velocity. One technique is simply distance divided by time, with time defined when amplitude first increased to a 10% threshold of peak amplitude and distance is the sample distance between the transducers. Increased accuracy is obtained with calibration. Another technique is to use subsequent responses which for through-transmission is the distance between transducers (denoted as X) and the time interim for the wave to reflect back to the transmitter and then reflect back to the receiver ( $1X + 2X = 3X$ ) and using the pulse-overlap technique to estimate the delta time (Papadakis 1967).

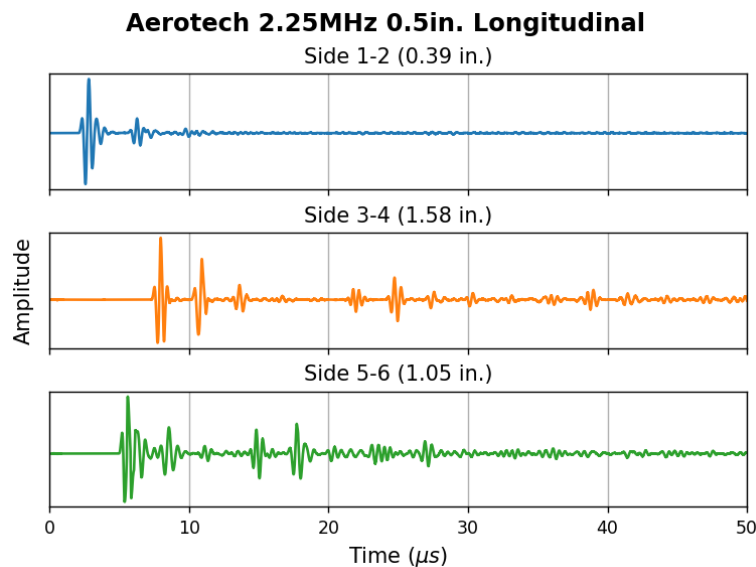


Figure 12. Amplitude versus time plots of the ultrasonic pulses for a 2.25 MHz longitudinal wave.

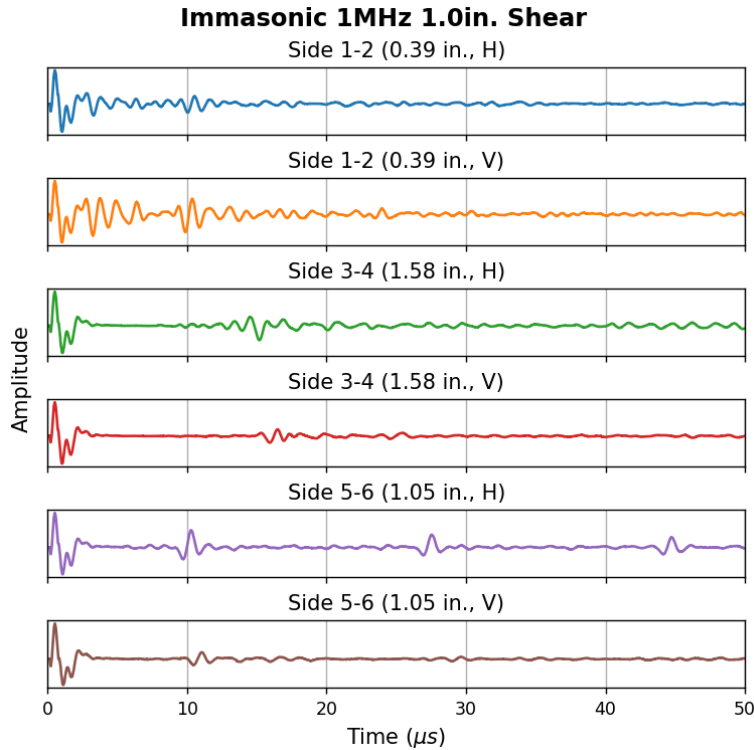
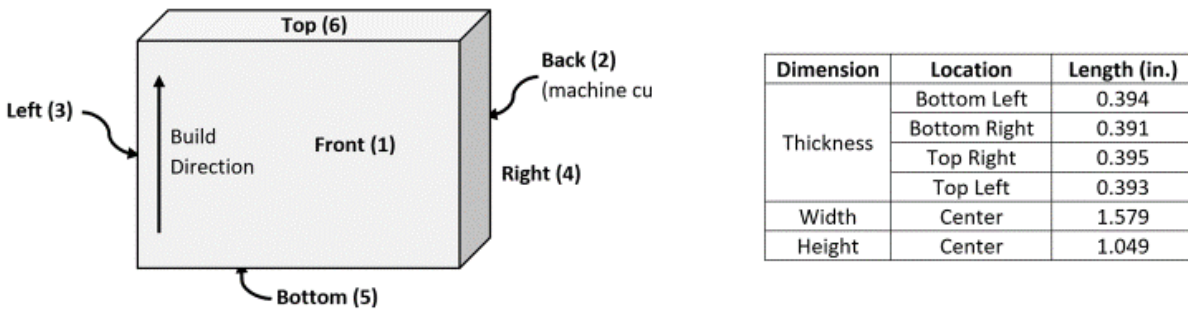


Figure 13. Amplitude versus time plots of the ultrasonic pulses for a 1.0 MHz shear wave.



A. Face Labels for Through-Transmission Measurements. B. Dimensions Measured from Specimen.

Figure 14. Face labeling (A) and dimensions (B) used for ultrasonic through-transmission measurements.

Due to the small sample size relative to the transducer diameter, mode conversion occurred which complicated the response pattern (Olsen and Pollock, 2009). S-wave measurements indicated additional complications from the polarized shear wave interacting with the sample sides. Less mode conversion was expected when particle motion is parallel to the sample sides than when perpendicular to the sample sides.

The longitudinal signal of transducers applied to sides 3 and 4, Figure 12 indicates a response at  $\sim 7.5 \mu\text{s}$  and  $\sim 22.5 \mu\text{s}$  for the 1.58 in direction as expected for the 1X and 3X pattern. The response train at  $10 \mu\text{s}$  and  $13 \mu\text{s}$  are believed to be mode converted waves (Olsen and Pollock, 2009). This pattern repeats for the second received L-wave. A similar pattern exists for the sides 5 and 6 data. For sides 1 and 2 data, the second L-wave response was not observed

and is assumed to be buried in noise. Since L-wave velocity is significantly faster than the S-wave, the first response is accepted as an L-wave and all mode conversions to the slower S-wave would lag behind. Thus, wave velocity by the  $V = X/\Delta t$  technique with calibration should be reasonably accurate. Use of pulse-overlap seems problematic since the second L-wave response was not always evident.

The shear signal of transducers applied to sides 5 and 6 with transducer at H orientation, Figure 13, indicated responses at  $\sim 9 \mu\text{s}$  and  $27 \mu\text{s}$  which matches the 1X and 3X criteria for pulse-overlap. Birefringence seems evident due to a slightly earlier arrival time for H orientation versus V orientation responses. The sides 3 and 4 oriented H seems to have an earlier arrival time than the oriented V response which reinforces the possibility of S-wave birefringence. Low level ultrasonic responses prior to the S-wave response around  $10 \mu\text{s}$  are assumed to be from mode conversion. The earlier arrival time is consistent with an L-wave by mode conversion of the S-wave. The L-wave higher wave velocity would result in an earlier arrival time than the S-wave.

Due to inconsistencies, mode conversion, and loss of expected response pattern, care is needed to make measurements for either a pulse-echo or through-transmission techniques and properly interpret results. Although not well suited for small samples, these techniques offer greater flexibility such as in the field to accommodate larger materials volumes and non-optimal geometries such as a part curvature, non-parallel surfaces, or increased surface roughness [Brennan et al. 2020].

## 4.2 Resonance Ultrasound Spectroscopy Results

Approximately 30 resonance modes were measured for each of the four wrought 316L cuboids as shown in Figure 15. While the entire frequency range between 135 to 350 kHz was analyzed, only discrete sections are shown. This was done for several reasons. First, it saved time when recording at higher resolutions when no signal was detected. Second, some resonant frequencies were higher amplitude than others and the signal needed to be attenuated to avoid saturation. If the entire frequency range was attenuated, then smaller amplitude resonances would be missed. By breaking up the frequency range into bands, only the high amplitude signals needed to be attenuated. Third, sometimes the sample needed to be adjusted to better resolve resonant peaks. If this was the case, then the sample need only be adjusted in specific bands, instead of the entire frequency range. This slight variation in response is due to different modes being a contribution of longitudinal, shear, and torsional motions and different probe positionings better lend to detecting different modes.

After the frequency response was collected. The modal frequencies were selected using the *findpeaks* function in the SciPy Python (high-level, general-purpose programming language) module. After the resonance frequencies were measured, they were matched to the ones calculated in the forward problem. Interestingly, the expected resonance frequency for Mode 6 was not observed in any of the measurements of the cuboids. Various sample and probe orientations were used to try and detect the resonance. One explanation is that the drive signal was attenuated by 30db and 24db for Modes 5 and 7 to avoid signal saturation. It is likely Mode 6 had a smaller response compared to Modes 5 and 7 and was overshadowed by their greater response. Due to this, Mode 6 was not used to fit the RUS model leaving only 29 modes out of the expected 30. The resulting RUS fit for isotropic and hexagonal symmetries is shown in Appendix A. For the wrought cuboids, the RUS fit had an average percent difference of 0.735% between measured and predicted resonance frequencies for the isotropic model and 0.655% for the hexagonal model.

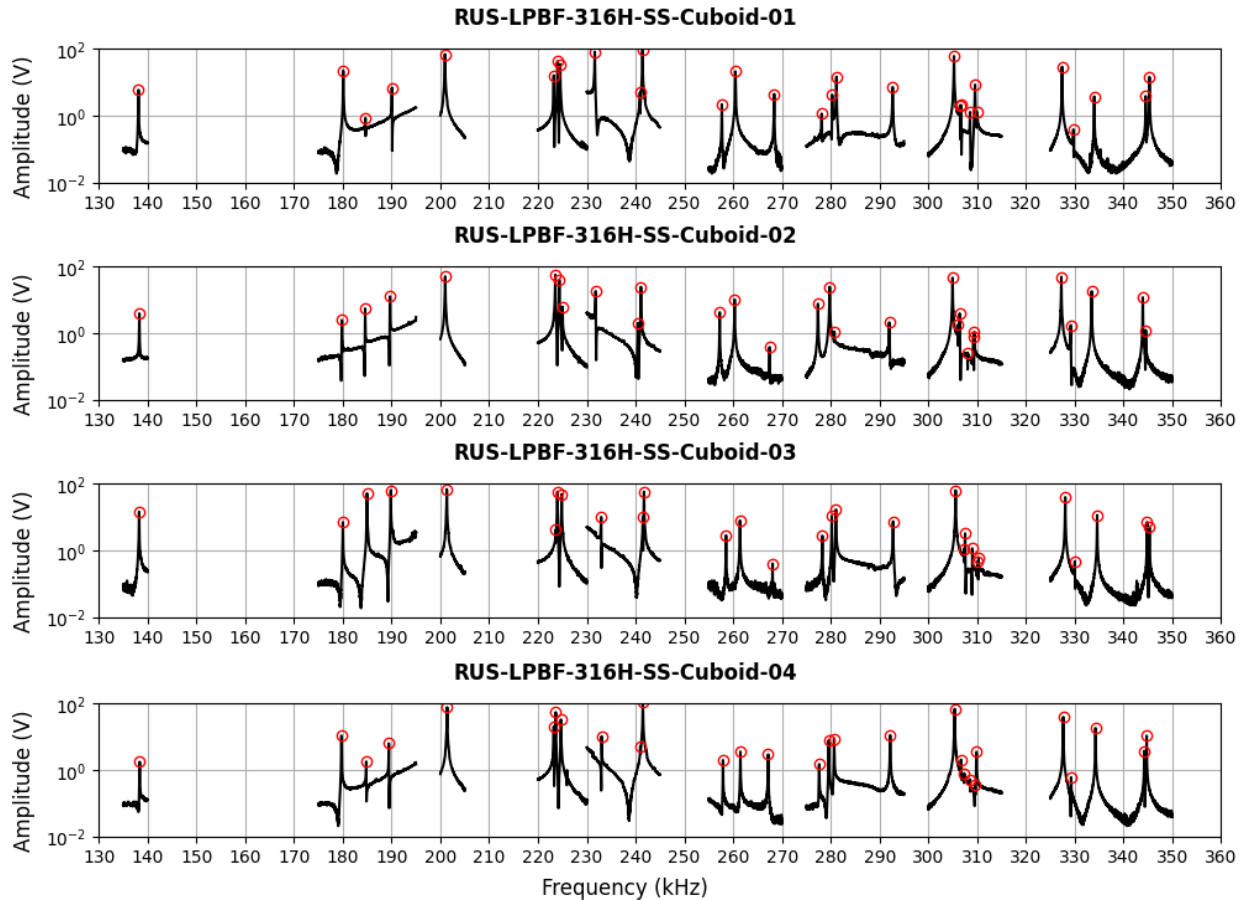


Figure 15. Resonant frequencies (black line) from Wrought 316L Cuboids and the identified modal peaks (red circles).

The same process of measuring the resonance frequencies was performed on the LPBF 316H samples (See Figure 16). Overall, the predicted resonance frequencies in the forward model resulted in a very similar grouping of resonance frequencies (see Appendix A). Mode 6, while not observed in the wrought 316L samples was observed in the LPBF 316H samples. It is unclear why Mode 6 was resolved in the LPBF samples and not the wrought 316L. Modes 21-23 were grouped much closer together in the LPBF samples than in the wrought 316L cuboids. This resulted in some of the modes not being resolved in the experimental measurement. For Cuboids 1 and 4, Mode 23 was missing while for Cuboids 2 and 3, Mode 22 and 23 were missing. This can happen when the modes are too close together in frequency to be able to be distinguished as separate. As a result, only 28 and 29 frequencies were used to fit the RUS model for Cuboids 2 and 3 and 1 and 4, respectively. On average the RUS fit had an average error of 0.341% for the isotropic model and 0.234% for the hexagonal model.

The resulting elastic constants and bulk properties from the RUS fit are shown in Table 7 for the isotropic model and Table 8 for the hexagonal model.

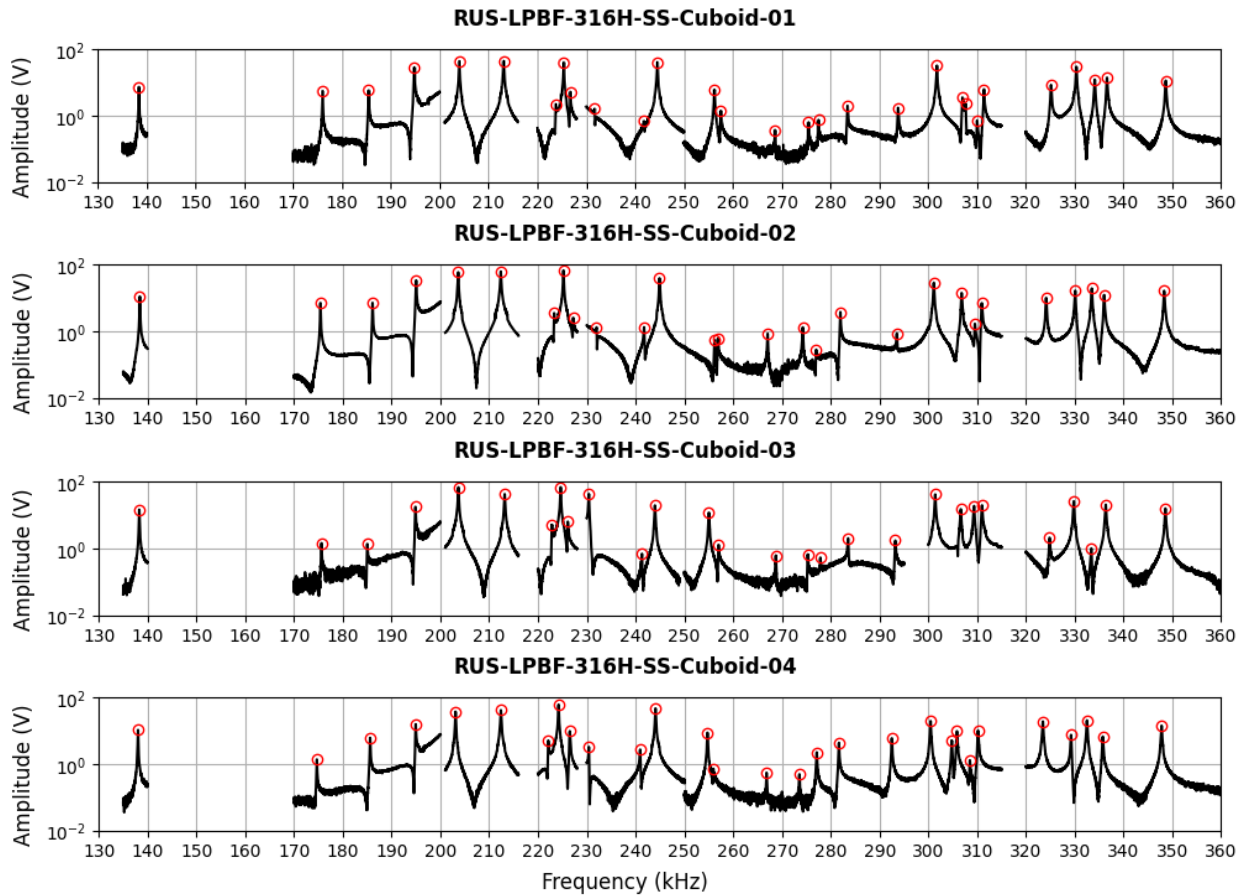


Figure 16. Resonant frequencies (black line) from LPBF 316H Cuboids and the identified modal peaks (red circles).

Table 7. Single-crystal elastic constants and resulting bulk elastic properties for the isotropic RUS model.

	Wrought 316L				LPBF 316H			
	Cuboid 1	Cuboid 2	Cuboid 3	Cuboid 4	Cuboid 1	Cuboid 2	Cuboid 3	Cuboid 4
<b>C11 (GPa)</b>	247.77	248.73	248.18	249.24	259.07	258.65	261.60	256.75
<b>C12 (GPa)</b>	94.34	95.13	95.03	95.90	107.62	106.72	110.24	106.59
<b>C44 (GPa)</b>	76.72	76.80	76.57	76.67	75.73	75.96	75.68	75.08
<b>Bulk M (K) (GPa)</b>	145.48	146.33	146.08	147.01	158.10	157.36	160.69	156.65
<b>Shear M (G) (GPa)</b>	76.715	76.803	76.574	76.672	75.727	75.963	75.683	75.08
<b>Youngs M (E) (GPa)</b>	195.74	196.10	195.55	195.95	195.90	196.30	196.24	194.21
<b>Poisson R</b>	0.2758	0.2766	0.2769	0.2779	0.2935	0.2921	0.2965	0.2934

Table 8. Single-crystal elastic constants and resulting bulk elastic properties for the hexagonal RUS model.

	Wrought 316L				LPBF 316H			
	Cuboid 1	Cuboid 2	Cuboid 3	Cuboid 4	Cuboid 1	Cuboid 2	Cuboid 3	Cuboid 4
<b>C11 (GPa)</b>	244.88	246.84	244.42	247.79	260.02	259.74	256.24	252.22
<b>C22 (GPa)</b>	244.88	246.84	244.42	247.79	260.02	259.74	256.24	252.22
<b>C33 (GPa)</b>	256.19	257.14	257.16	261.66	263.13	258.41	257.92	250.03
<b>C23 (GPa)</b>	98.84	100.12	99.19	103.80	110.18	106.41	105.52	100.05
<b>C13 (GPa)</b>	98.84	100.12	99.19	103.80	110.18	106.41	105.52	100.05
<b>C12 (GPa)</b>	89.86	92.44	89.66	92.83	110.99	109.99	107.30	103.49
<b>C44 (GPa)</b>	76.82	77.19	76.66	76.90	76.92	76.80	77.03	75.99
<b>C55 (GPa)</b>	76.82	77.19	76.66	76.90	76.92	76.80	77.03	75.99
<b>C66 (GPa)</b>	77.51	77.20	77.38	77.48	74.51	74.87	74.47	74.37
<b>Bulk M (K) (GPa)</b>	141.54	143.91	141.25	144.48	160.66	159.91	156.94	153.06
<b>Shear M (G) (GPa)</b>	77.51	77.198	77.382	77.482	74.514	74.872	74.471	74.366
<b>(GPa)</b>	197.83	198.05	198.25	198.40	197.68	197.17	196.66	193.74
<b>Youngs M - T (GPa)</b>	193.81	194.11	193.35	193.70	194.21	195.64	193.77	193.21
<b>Poisson R</b>	0.2953	0.2951	0.2969	0.3047	0.2970	0.2878	0.2903	0.2813

The Bulk Modulus, Shear Modulus, and Poisson's Ratio reported in Table 7 and Table 8 are shown in Figure 17 in several boxplots. The boxplot was constructed by using the calculated values for each of the four cuboids to plot the distribution of values for a given material type and RUS model used. The Wrought 316L material was expected to have isotropic symmetry and, of the four groups shown, the isotropic model has the least variation in elastic properties. Interestingly, the hexagonal model for the wrought 316L has a decreased Bulk modulus and increased Shear Modulus and Poisson's ratio. It is unclear why this is the case as the hexagonal model should provide the same results as the isotropic model for an isotropic material. This could be caused by a strong rolling direction in the 316L. The manufacturer was contacted to acquire more precise material information about the rolling direction but a response was not received in time for this report.

The LPBF 316H cuboids have a noticeably increased Bulk modulus and Poisson's ratio and a decreased Shear modulus compared to the wrought 316L calculated from the isotropic RUS model. The LPBF 316H material was not expected to behave isotropically so it is not surprising that the isotropic and hexagonal models result in slightly different elastic properties (unlike for the wrought 316L material). Additionally, the distribution of the 316H cuboids is larger for the hexagonal model than the isotropic model. It is important to note that the hexagonal RUS fit actually has the smallest average error between measured and predicted resonance

frequencies of only 0.234%. The best explanation to this indicates that the actual LPBF has anisotropic material properties that vary spatially.

Literature suggests that LPBF parts are typically most equiaxed nearest the build plate with more columnar grains occurring as more and more of the part is built [DebRoy et al., 2018]. This is mainly due to grain growth occurring along the direction of greatest temperature gradient. At the beginning of the part, the build plate acts as a heatsink which cools the part rapidly resulting in smaller, equiaxed grains. However, as more of the part is built more heat is retained and the part cools more slowly resulting in columnar grains oriented in the build direction. Due to this phenomenon, it was expected that Cuboids 3 and 4 (nearest to the build plate) would behave more isotropically than Cuboids 1 and 2 (farthest from the build plate). Cuboid 04 does appear to support this theory with the Young's moduli in the longitudinal and transverse directions being nearly identical. However, Cuboid 03 did not behave isotropically but instead has a Young's Modulus that varies depending on the orientation. This may be related to the fact Cuboid 03 having a lower density than the other 3 cuboids but more work will need to be performed to confirm this. Cuboids 1 and 2 behave as expected with the bulk properties in the longitudinal direction varying from that of the transverse direction. These results are promising for using RUS to evaluate AM parts with complex microstructures but do indicate that future work will need to have a better understanding of the microstructure of the RUS specimens.

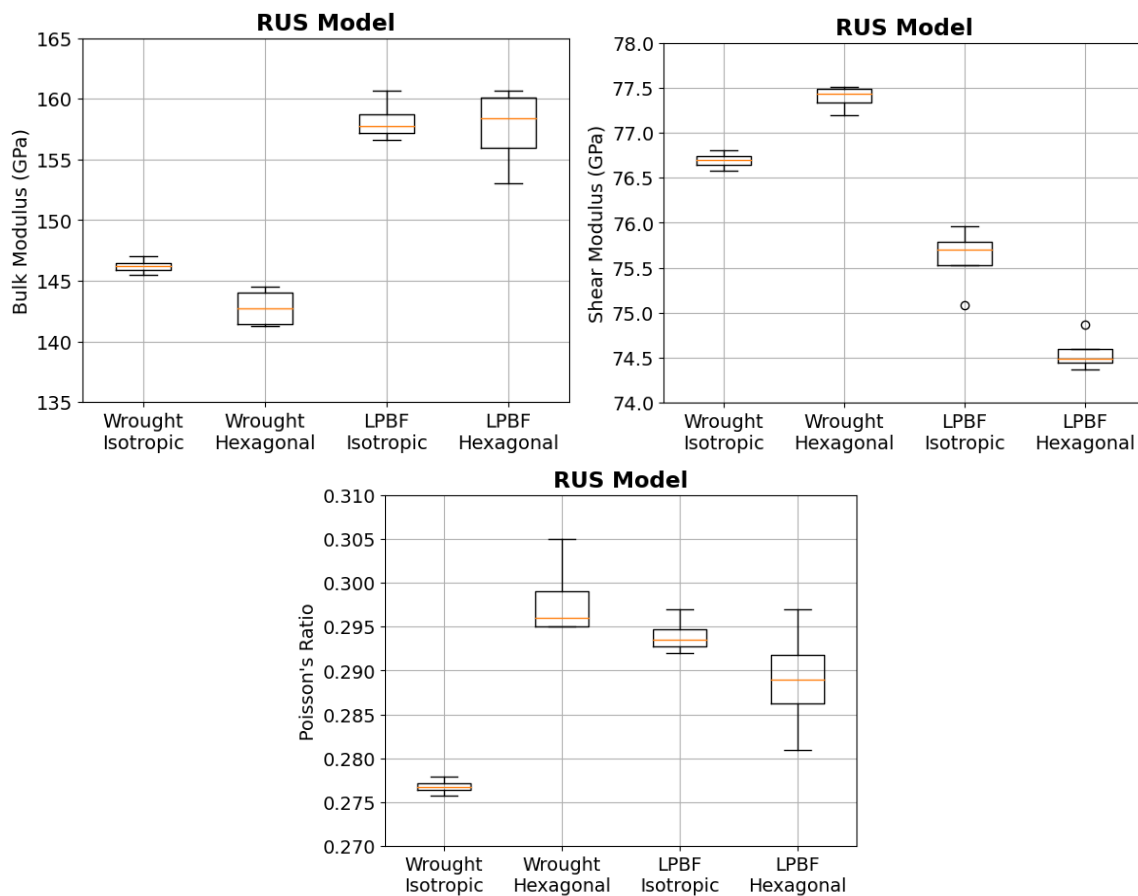


Figure 17. Bulk Modulus, Shear Modulus, and Poisson's Ratio for each material and RUS model used for the four cuboids.

### 4.3 Tensile Testing Results

The tensile test results are summarized in Table 9 for the ASTM E8 sub-size wrought 316L specimens. Due to difficulties in performing the tensile tests using the SS-J3 specimens, these results were not available at the time the report was prepared. Once these results become available, the report will be updated.

The ASTM E8 subsize specimens were tested to specimen failure and results are provided for the ultimate tensile stress (UTS), Yield Stress (YS), and Young's Modulus. As noted in the table, the Young's Modulus displays an orientation dependence between the vertical and horizontal specimens. The values for the horizontal specimens ranges between 172 to 185.7 GPa. The vertical specimens have values that range between 190.7 to 199.3 GPa. Information on the fabrication of the Wrought 316L material was not available at the time the report was prepared. Since the original source was plate geometry, a rolling processing step is likely that may have affected the Young's Modulus.

Table 9. Mechanical Testing Results for the ASTM E8 Subsize Wrought 316L Specimens

Specimen	Ultimate Tensile Strength (MPa)	Yield Stress (MPa)	Young's Modulus (GPa)
Horizontal 1-1	599.0	285	185.7
Horizontal 1-2	602.6	285	174.4
Horizontal 1-3	587.6	246	172.0
Vertical 1-1	604.3	301	199.3
Vertical 1-2	601.2	254	190.7
Vertical 1-3	592.2	295	197.9

### 4.4 Comparison of RUS and Tensile Testing Results

The comparison of the Young's Modulus obtained from the RUS measurements with the results from the tensile testing of the wrought 316L material is shown in Figure 18. Good agreement is seen in the elastic modulus measured in the vertical direction of the wrought plate. Differences are noted in the comparison with the horizontal specimens. Information on the wrought 316L plate fabrication parameters was not available at the time the report was written. It is possible that the horizontal specimens aligned with rolling forming processes.

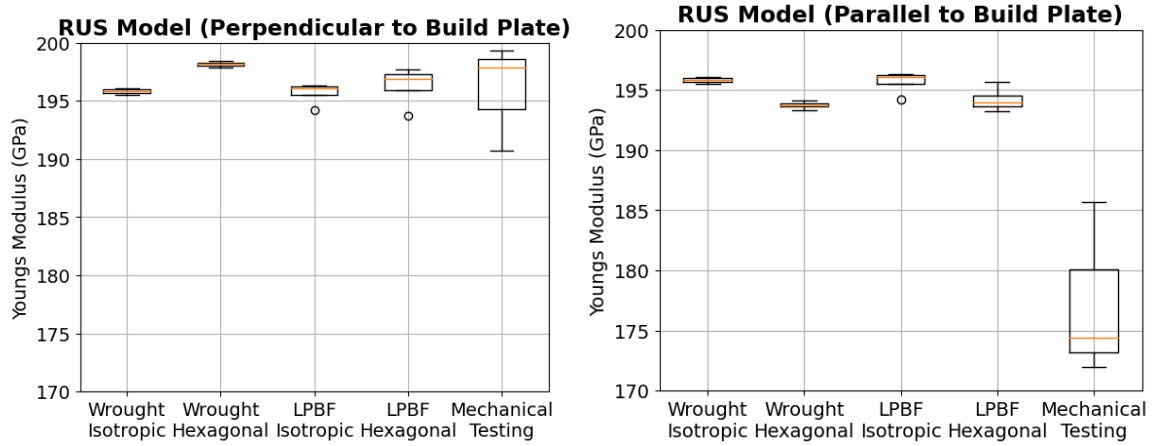


Figure 18. Youngs Modulus for each material type and RUS model used for all cuboids compared with tensile testing of three wrought 316L specimens.

## 5.0 Observations and Next Steps

The preliminary results from recent experiments performed to evaluate the capability of advanced UT techniques to interrogate and confirm the material properties in LPBF SS 316 H have shown the following:

- The RUS measurements found the Bulk Modulus is ~10% higher for the LPBF SS 316 H material as compared to the wrought 316L.
- A weak elastic anisotropy was observed in the LPBF material using the preliminary RUS measurements and the hexagonal crystallographic model. Refinements in this method are needed.
- For a polycrystalline material with isotropic elasticity preliminary RUS measurements did not indicate significant differences in wrought equiaxed grain microstructure and the as-received LPBF material with the nonuniform grain structure.
- Mechanical testing using SS-J3 specimens showed high variability in the elastic modulus determination and requires further improvements in the methodology before comparison to RUS can be made.

Further work will include the following actions:

- Improved mechanical testing is needed to reliably measure the elastic modulus from the SS-J3 specimens.
- While application of RUS methods to measure the impact of LPBF manufacturing on the elastic constants and engineering elastic modulus showed promising results, further work is needed to understand the impact of microstructural effects.
- Consideration will be given to advanced ultrasonic bulk waves, backscatter and/or attenuation methods to provide additional information on the microstructural features and defect detect [Guo and Todd, 2022].
- Obtain additional SS 316H material (both wrought and LPBF) with well characterized microstructure. A variety of LPBF process parameters with different microstructure features/characteristics is needed to understand detectability of these features with ultrasound-based methods.

## 6.0 References

- Asmani M., Kermel C., Leriche A., Ourak M.. 2001. Influence of porosity on Young's modulus and Poisson's ratio in alumina ceramics, *Journal of the European Ceramic Society*, Volume 21, Issue 8, Pages 1081-1086. [https://doi.org/10.1016/S0955-2219\(00\)00314-9](https://doi.org/10.1016/S0955-2219(00)00314-9)
- Brennan, R, M Golt, and M Ivill. 2020. Comparison of Dynamic Methods for Determining Elastic Property Measurements of Solid Materials, report ARL-TR-9130, DEVCOM Army Research Laboratory, Aberdeen Proving Ground, MD, <https://apps.dtic.mil/sti/pdfs/AD1120254.pdf>
- DebRoy T., Wei H.L. Zuback J.S., Mukherjee T., Elmer J.W., Milewski J.O., Beese A.M., Wilson-Heid A., De A., Zhang W. 2018. Additive manufacturing of metallic components – Process, structure and properties, *Progress in Materials Science*, 92: 112-224. <https://doi.org/10.1016/j.pmatsci.2017.10.001>
- Dieulesaint E. and Royer D.1980. *Elastic Waves in Solids*, John Wiley and Sons Ltd.
- Garlea E., Choo H., Sluss C.C., Koehler M.R., Bridges R.L., Xiao X., Ren Y., Jared B.H. 2019. Variation of elastic mechanical properties with texture, porosity, and defect characteristics in laser powder bed fusion 316L stainless steel, *Materials Science and Engineering: A*, Volume 763, 138032, ISSN 0921-5093, <https://doi.org/10.1016/j.msea.2019.138032>.
- Goebbels, K. 1980. Chapter 4, Structure Analysis by Scattered Ultrasonic Radiation, in *Research Techniques in Nondestructive Testing*, Vol. IV. ed: RS Sharpe. Academic Press, Inc., New York, <https://www.osti.gov/etdeweb/biblio/7043656>.
- Guo y. and Todd, D. 2022, Agile MCPC Specimens Characterization with NDE Method, PNNL-SA-179036.
- Gussev, Maxim N., Busby, Jeremy T., Field, Kevin G., Sokolov, Mikhail A., and Gray, Sean E. 2014 “Role of Scale Factor During Tensile Testing of Small Specimens,” *Small Specimen Test Techniques: 6th Volume*, STP 1576, Mikhail A. Sokolov and Enrico Lucon, Eds., pp. 1–19, ASTM International, West Conshohocken, PA. <https://doi.org/10.1520/STP157620140013>.
- Honarvar F. and Varvani-Farahani, A. 2020. A review of ultrasonic testing applications in additive manufacturing: Defect evaluation, material characterization, and process control, *Ultrasonics* 108, 106227, <https://doi.org/10.1016/j.ultras.2020.106227>.
- Huang N., Cook O.J., Smithson R.L.W., Kube C. M., Argüelles A. P., Beese A. M., 2022. Use of ultrasound to identify microstructure-property relationships in 316 stainless steel fabricated with binder jet additive manufacturing, *Additive Manufacturing*, Volume 51, 102591, <https://doi.org/10.1016/j.addma.2021.102591>.
- Jacob, R., et al. 2020, Survey of Pre-Service and In-Service Nondestructive Evaluation Techniques of AMT-Fabricated Components, PNNL-30759, United States Nuclear Regulatory Commission TLR-RES/DE/CIB-2020-12, [ML20349A012](https://www.osti.gov/etdeweb/biblio/1602349).
- Kim C., Yin H., Shmatok H., Prorok B.C., Lou X., Matlack K.H. 2021, Ultrasonic nondestructive evaluation of laser powder bed fusion 316L stainless steel, *Additive Manufacturing*, Volume 38, 101800, <https://doi.org/10.1016/j.addma.2020.101800>.

Ledbetter H. M., Weston W. F., Naimon E. R.. 1975. Low-temperature elastic properties of four austenitic stainless steels. *Journal of Applied Physics* 1 September 1975; 46 (9): 3855–3860. <https://doi.org/10.1063/1.322182>.

Leisure G. and Willis F. A. 1997 *J. Phys.: Condens. Matter* 9 6001. <https://doi.org/10.1088/0953-8984/9/28/002>.

Li, M., Andersson D., Dehoff, R., Jokisaari, A., Van Rooyen, I., and Cairns-Gallimore, D. 2022. Department of Energy Office of Nuclear Energy Advanced Materials and Manufacturing Technologies (AMMT) 2022 Roadmap, Report ANL-23/12, Argonne National Laboratory, Lemont, IL, <https://www.energy.gov/sites/default/files/2023-03/ne-ammt-roadmap-030823.pdf>.

Manogharan P., Rivière J. and Shokouhi P. 2022. Toward In-situ Characterization of Additively Manufactured Parts Using Nonlinear Resonance Ultrasonic Spectroscopy, *Research in Nondestructive Evaluation*, 33:4-5, 243-266, <https://doi.org/10.1080/09349847.2022.2103219>.

Olsen, K and D Pollock. 2009. Ultrasonic detection of simulated corrosion in 1 inch diameter steel tieback rods. Report TNW2009-07, Transportation Northwest, University of Washington, Seattle, WA, <https://rosap.ntl.bts.gov/view/dot/17240> .

Papadakis, EP. 1967. Ultrasonic Phase Velocity by the Pulse-Echo-Overlap Method Incorporating Diffraction Phase Corrections. *J Acoust Soc Am*, 1967, vol. 42, pp. 1045–1051. <https://doi.org/10.1121/1.1910688> .

Radovic, M, E Lara-Curzio, and L Riester. 2004. Comparison of different experimental techniques for determination of elastic properties of solids, *Materials Science and Engineering: A*, Vol. 368, 2004, pp. 56-70, <https://doi.org/10.1016/j.msea.2003.09.080> .

Sotelo L.D., Hadidi H., Pratt C.S., Sealy M.P., Turner J.A. 2021, Ultrasonic mapping of hybrid additively manufactured 420 stainless steel, *Ultrasonics*, 110, 106269, <https://doi.org/10.1016/j.ultras.2020.106269>.

Todorov, E, R Spencer, S Gleeson, M Jamshidinia, and SM Kelly. 2014. AMERICA MAKES: NATIONAL ADDITIVE MANUFACTURING INNOVATION INSTITUTE (NAMII) Project 1: Nondestructive Evaluation (NDE) of Complex Metallic Additive Manufactured (AM) Structures, Report AFRL-RX-WP-TR-2014-0162, Air Force Research Laboratory Materials and Manufacturing Directorate, Wright-Patterson Air Force Base, OH, <https://apps.dtic.mil/sti/pdfs/ADA612775.pdf> .

Torres J., Flores-Betancourt A., Hermann R. P. 2022. RUScal: Software for the analysis of resonant ultrasound spectroscopy measurements. *J Acoust Soc Am* 1 May 2022; 151 (5): 3547–3563. <https://doi.org/10.1121/10.0011397>

Visscher, W. M., Migliori, A., Bell, T. M., & Reinert, R. A. 1991. On the normal modes of free vibration of inhomogeneous and anisotropic elastic objects. *The Journal of the Acoustical Society of America*, vol. 90, issue 4, pp. 2154-2162 <https://doi.org/10.1121/1.401643>.

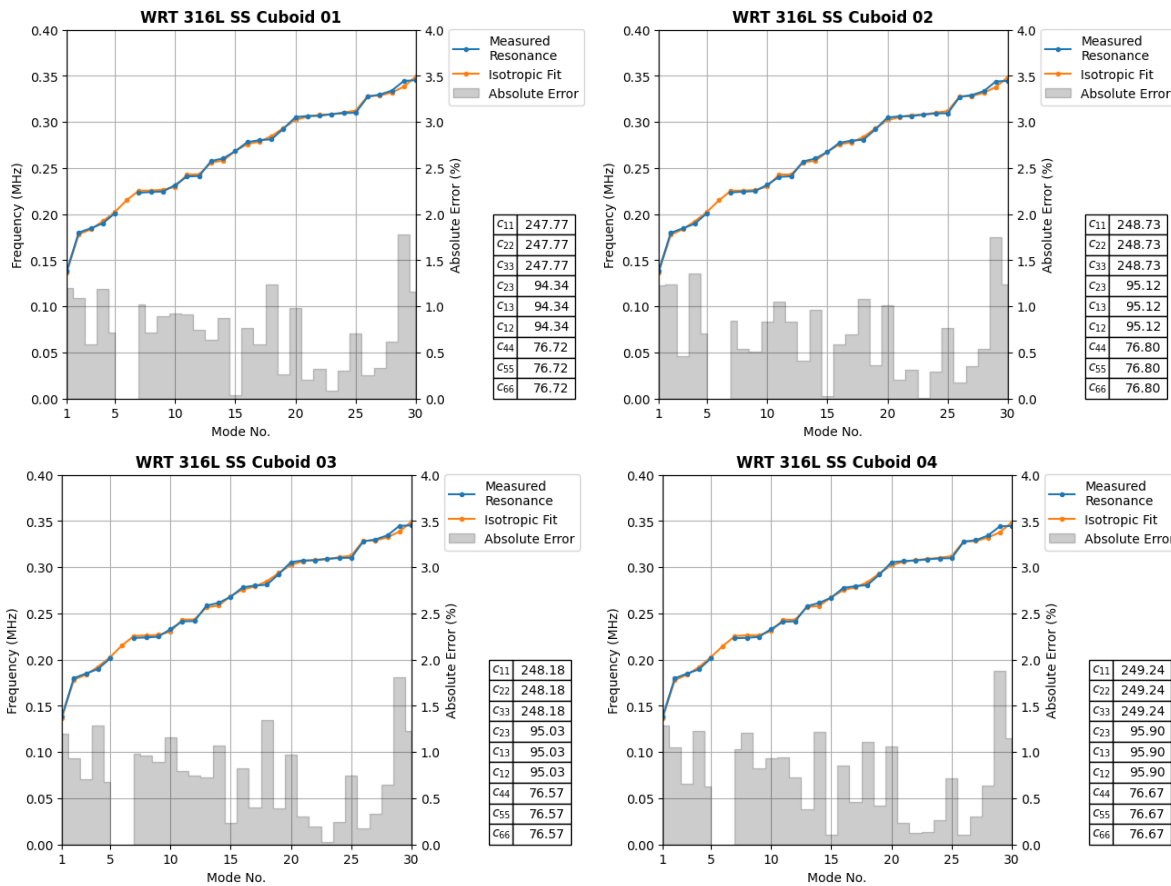
Waller, JM, BH Parker, KL Hodges, ER Burke, and JL Walker. 2014. Nondestructive Evaluation of Additive Manufacturing State-of-the-Discipline Report, Report NASA/TM—2014–218560, NASA Langley Research Center, Hampton, VA, <https://ntrs.nasa.gov/citations/20140016447> .



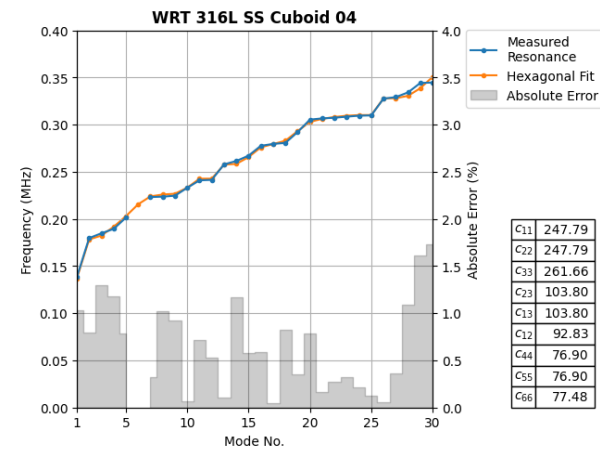
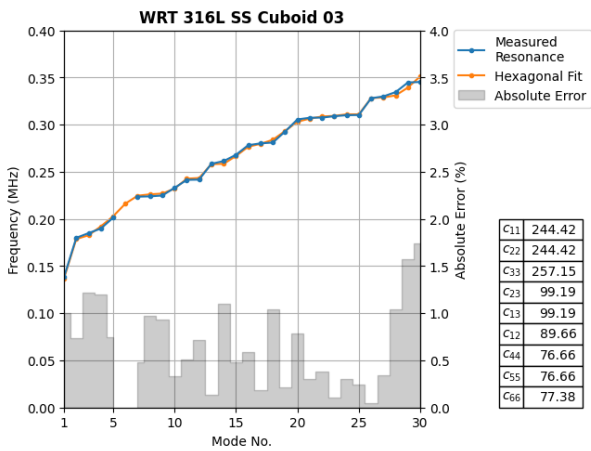
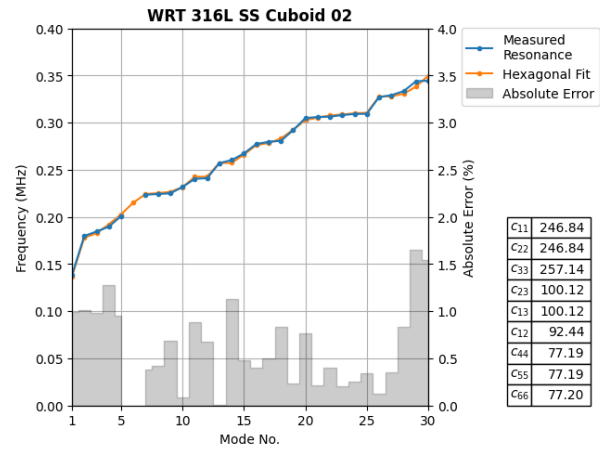
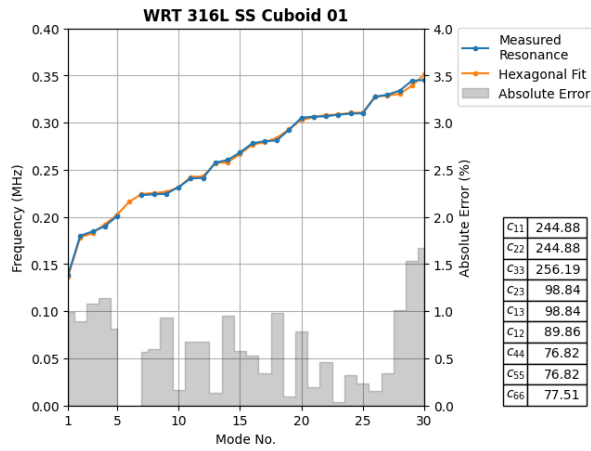
## Appendix A – RUS Frequency Spectrum and Model Fit Results

This appendix contains the resonance frequencies as a function of mode number obtained from the PNNL RUS system on the wrought 316 L and LPBF 316 H cuboid specimens. The results for both the isotropic and hexagonal (or transversely isotropic) models are shown for comparison. The absolute error between the measured frequencies and the model predictions are also included in the figures.

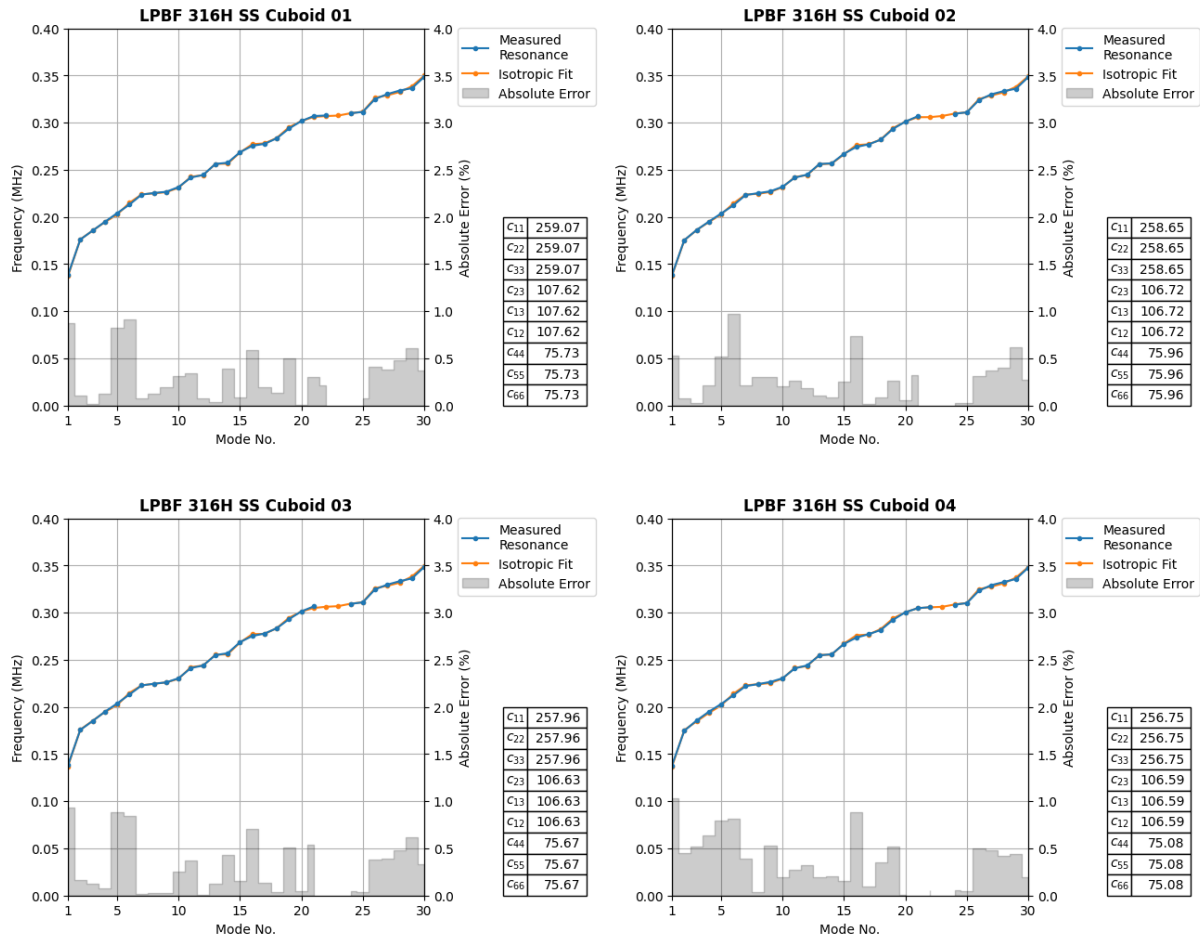
### A.1 Wrought 316 L with Isotropic Model



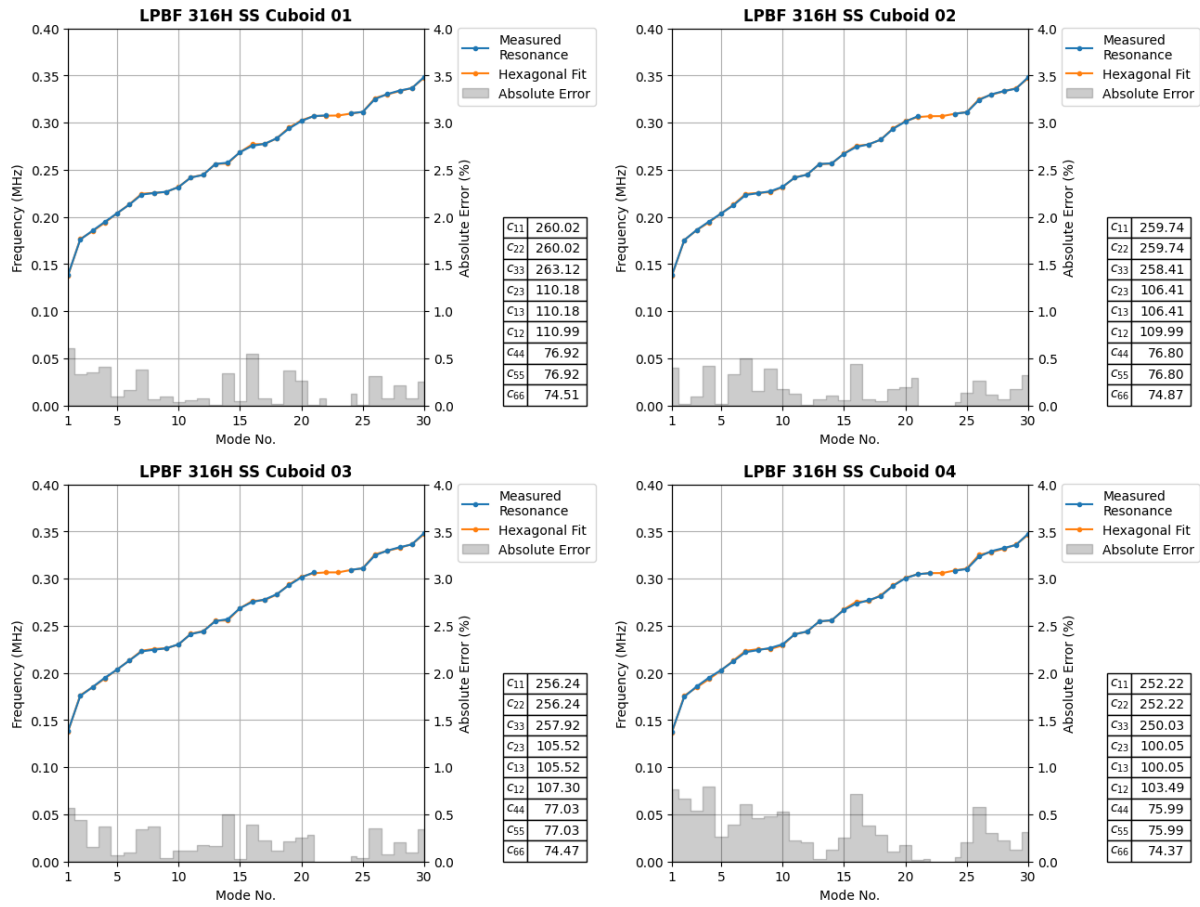
## A.2 Wrought 316 L with Hexagonal Model



### A.3 Laser Power Bed Fusion 316 H Isotropic Model



## A.4 Laser Power Bed Fusion 316 H Hexagonal Model



# **Pacific Northwest National Laboratory**

902 Battelle Boulevard  
P.O. Box 999  
Richland, WA 99354  
1-888-375-PNNL (7665)

***[www.pnnl.gov](http://www.pnnl.gov)***